Supporting Information

Ultrasensitive Dim-Light Neuromorphic Vision Sensing via Momentum-Conserved Reconfigurable van der Waals Heterostructure

Lei Xu, Junling Liu, Xinrui Guo, Shuo Liu, Xilin Lai, Jingyue Wang, Mengshi Yu, Zhengdao Xie, Hailin Peng, Xuming Zou, Xinran Wang, Ru Huang, and Ming He

Supplementary Notes

Supplementary Note 1: DFT Calculation for Energy Band

The first-principles density functional theory (DFT) calculations were conducted using the Vienna Ab Initio Simulation Package (VASP). The electron-ion interactions were characterized by the Projected Augmented Wave (PAW) method. Geometry optimization employed the Generalized Gradient Approximation (GGA) with the Perdew-Burke-Ernzerhof (PBE) exchange-correlation functional, incorporating a plane-wave basis set cutoff of 500 eV for both Bi_2O_2Se and $MAPbI_3$, with the latter crystallizing in the *Pnma* space group. The Brillouin zone integration was facilitated by the Monkhorst-Pack (M-P) *k*-point meshes of 13×13×6 for Bi_2O_2Se and 10×8×6 for $MAPbI_3$. Convergence criteria for electronic self-consistency were set at a total energy precision within 10^{-4} eV, while the Hellmann-Feynman forces were constrained below 10^{-2} eVÅ^{-1}. The resulting equilibrium lattice parameters, a = b = 3.92 Å and c = 12.39 Å for Bi_2O_2Se, and a = 8.56 Å, b = 9.28 Å, and c = 12.90 Å for $MAPbI_3$, align closely with experimental values.[1,2] To address the proclivity of PBE method for bandgap underestimation, we applied the modified Becke-Johnson potential coupled with spin-orbit interaction for bandgap calculations.[3-5] The resulted bandgaps (i.e., 0.86 eV for Bi_2O_2Se, and 1.4 eV for $MAPbI_3$) were corroborated by the modulation parameters of 1.28 and 1.4, respectively, are very close to the experimental data.

Supplementary Note 2: Quantifying Light Brightness and Human Vision

Illuminance, measured in lux, serves as a metric for the perceived brightness of light by the human eye, and is defined as luminous flux per unit area. This relationship is underpinned by the formula: luminous flux = constant × human eye spectral luminous efficiency function × radiant power.[6] Specifically, at the peak sensitivity wavelength of the human eye (i.e., 555 nm), a radiant power of 1 W is equivalent to a luminous flux of 683 lm, given the human eye spectral luminous efficiency function of 1. This equivalence establishes that 1 lux corresponds to 1 lm/m^{-2}, that is 1/683 wm^{-2} of green light. Therefore, an illuminance of 0.1 μWcm^{-2} translates to approximately 0.68 lux, evocative of the natural moonlight.[7]

Supplementary Note 3: Preprocess for Recognizing Traffic-Light Color

For the image processing and convolutional neural networks (CNNs), convolutional kernels play a pivotal role in tasks such as image blurring, sharpening, edge detection, and the extraction of salient features (e.g., edges, textures, and patterns). These kernels are instrumental in discerning specific attributes within images, thereby facilitating a nuanced understanding and manipulation of visual data. Fig. 5a illustrates the implementation of three quintessential convolutional kernels. The inaugural function, inversing, serves as a stylization technique, transforming the visual aesthetics of an image. Subsequently, the denoising function, characterized by its operator weights arranged in accordance with the 2D Gaussian distribution $G = \frac{1}{2\Pi\sigma^2} e^{-\frac{x^2+y^2}{2\sigma^2}}$, is colloquially termed Gaussian blur due to its efficacy in blurring and noise reduction. The terminal function, dedicated to edge detection, employs a discrete form of Laplacian operator $L(x,y) = \frac{\partial^2 I}{\partial x^2} + \frac{\partial^2 I}{\partial y^2}$, where $L(x,y)$ is the operator and I is the pixel intensity of images. The Laplacian operator, characterized by its 2D isotropic measure of the second-order spatial derivative, exhibits high sensitivity to noise, thereby necessitating a preliminary denoising phase to optimize the clarity and precision of edge detection.

We employed a 3×3 sensor array to formulate a Gaussian filter operator, aimed at denoising images marred by noise. For the task of traffic-light detection, where the input images feature three RGB channels, we executed a convolution of each RGB channel individually with the Gaussian kernel. The images in the LISA Traffic Lights dataset possess a resolution of 1280×960 pixels, and to simulate realistic conditions, we introduced Gaussian noises to these images prior to their use in the traffic light recognition task. The Gaussian smoothing convolution operator in the size of 3×3 was designed based on the distribution patterns of a 2D Gaussian function, ensuring that the center pixel exerts the most significant influence on the outcome, with a progressively diminishing contribution from the peripheral pixels. This design facilitates a smoothing effect, with a typical discrete approximation of the weight distribution depicted in Fig. 5a, displaying the center: edge: corner weight ratio of 4:2:1 for the 3×3 matrix.

Given the tri-channel nature of the input images, we deployed three distinct 3×3 operators tailored for the red, green, and blue channels, respectively. For the red channel, a 780 nm wavelength was chosen, adjusting the biases for the central, edge, and corner pixels within the 3×3 sensor array to V_g=-1.3 V, -0.8 V, and -0.7 V, respectively. This resulted in varying photoresponsivity R of 1.0×10^7 AW^{-1}, 5.0×10^6 AW^{-1}, and 2.5×10^6 AW^{-1}, respectively. Similarly, wavelengths of 532 nm and 400 nm were selected for the green and blue channels, with the sensor arrays configured accordingly to serve as convolution kernels in image processing. In subsequent simulations, the input images were dissected into their constituent RGB channels, with pixel values linearly transformed from the 0-255 range to correspond to an incident light intensity in the range of 1.5-150 μWcm^{-2}. A convolutional kernel was then applied by sliding it across the image, commencing with the initial 3×3 window, and employing a stride of 1. For each 3×3-pixel sub-window, the simulation computed the photocurrent $I_{ph}=\Sigma RP$, where P is the product of pixel value. The output value of each sliding window was then used as the pixel value for the corresponding position in the denoised output image.

Supplementary Figures

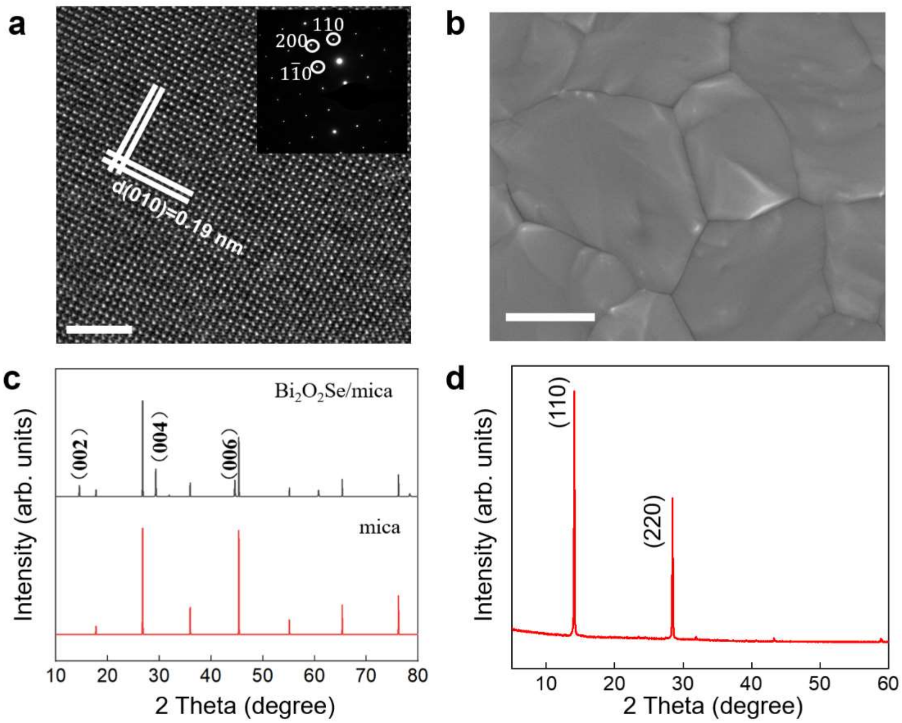

Supplementary Figure 1. Characterization of Bi_2O_2Se and $MAPbI_3$ films. (a) High-resolution transmission electron microscopy (TEM) image of Bi_2O_2Se film. The scale bar is 3 nm. (b) Top-view scanning electron microscopy (SEM) image of methylammonium lead iodide ($MAPbI_3$) perovskite film. The scale bar is 500 nm. X-ray diffraction pattern of (c) Bi_2O_2Se film and (d) $MAPbI_3$ film.

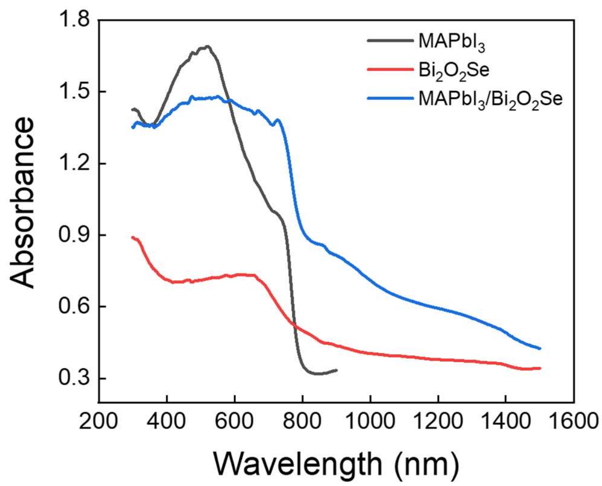

Supplementary Figure 2. Absorption spectra of $MAPbI_3$, Bi_2O_2Se and $MAPbI_3/Bi_2O_2Se$ films. Absorption spectra measured in the range of 300 nm to 1500 nm.

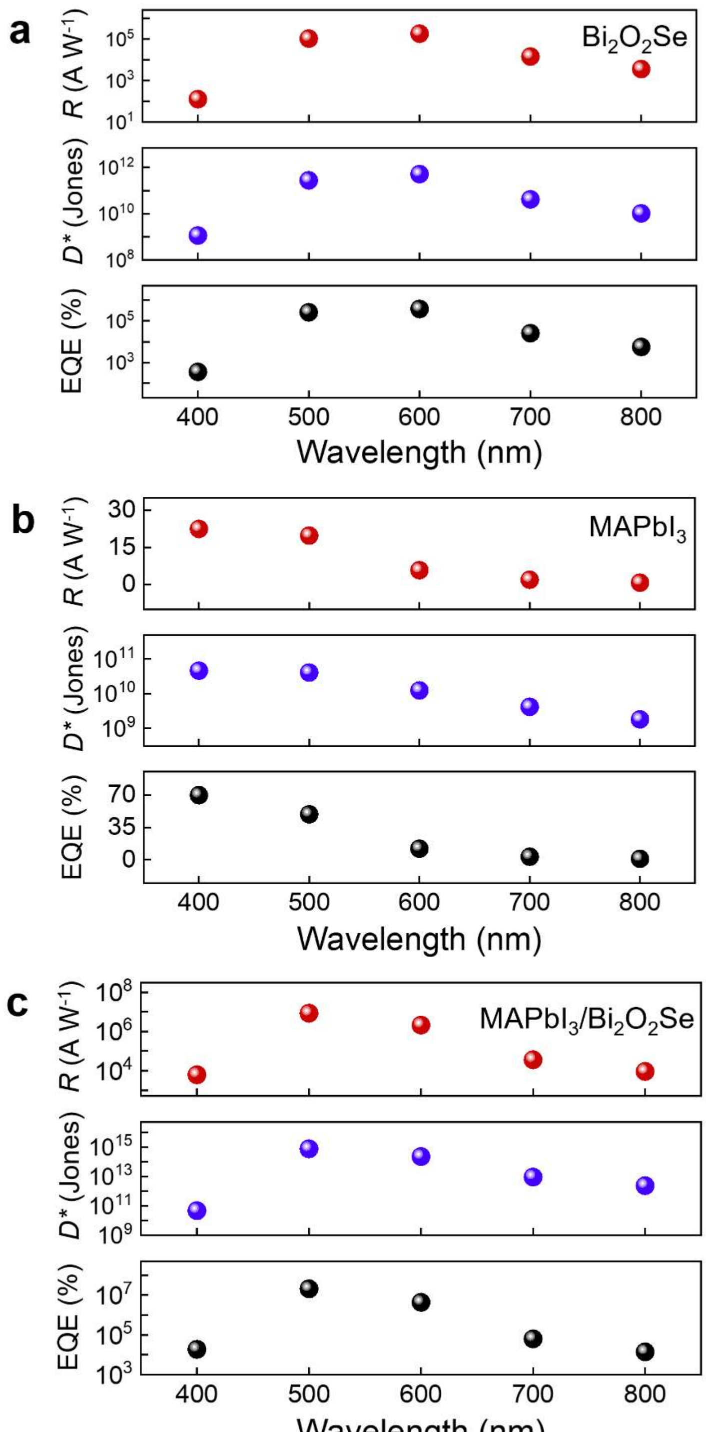

Supplementary Figure 3. Wavelength-dependent photoresponse characteristics. Wavelength dependence of photoresponsivity *R*, specific detectivity D^*, and external quantum efficiency EQE within (a) Bi_2O_2Se phototransistor, (b) $MAPbI_3$ phototransistor, and (c) $MAPbI_3/Bi_2O_2Se$ heterojunction phototransistor.

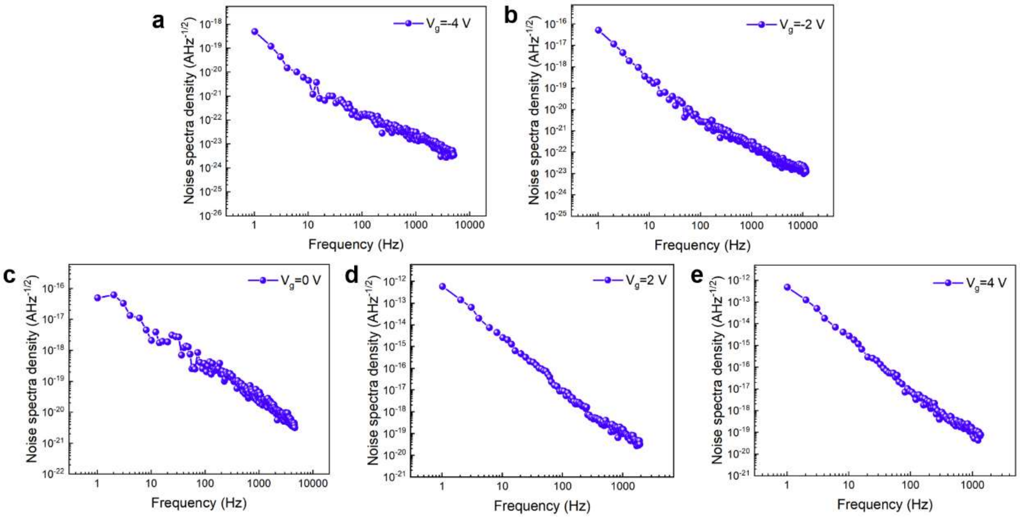

Supplementary Figure 4. Noise spectral density of the $MAPbI_3/Bi_2O_2Se$ heterotransistor. Noise spectral density of heterotransistor measured at the gate voltage of (a) V_g=-4 V, (b) V_g=-2 V, (c) V_g=0 V, (d) V_g=2 V, and (e) V_g=4 V.

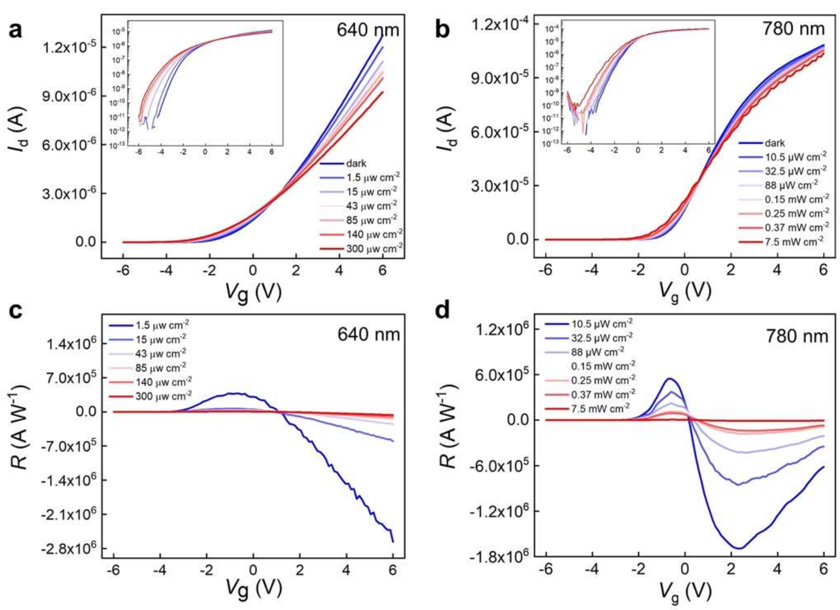

Supplementary Figure 5. Steady-state bipolar photoresponse of the heterotransistor. Transfer curves of $MAPbI_3/Bi_2O_2Se$ heterotransistor under the light illumination of (a) 640 nm and (b) 780 nm. The inset images show the transfer curves on a logarithmic scale. Positive and negative bipolar photoresponsivity dependence on the gate voltage of $MAPbI_3/Bi_2O_2Se$ heterotransistor under the light illumination of (c) 640 nm and (d) 780 nm.

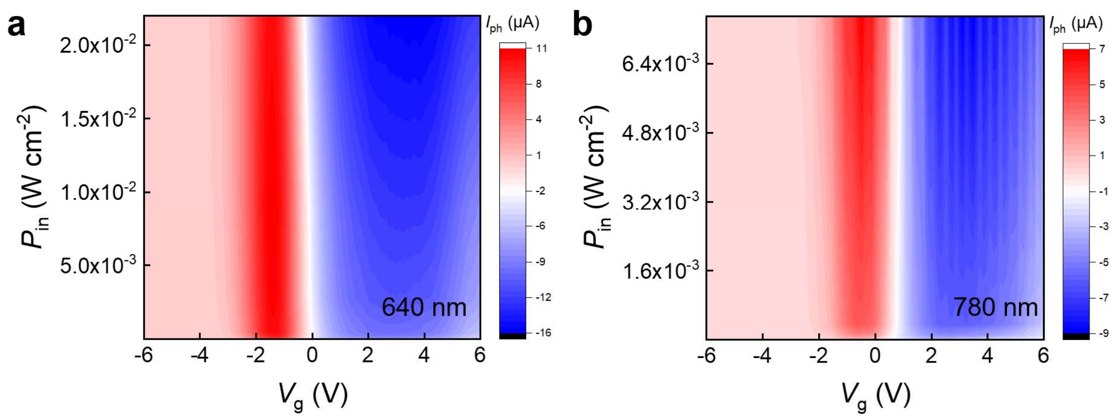

Supplementary Figure 6. Gate voltage-dependent bipolar photocurrent characteristics. Pseudo-color plots of the net photocurrent under the light illumination of (a) 640 nm and (b) 780 nm with varied light intensities, accompanied by the gate voltage from -6 V to 6 V.

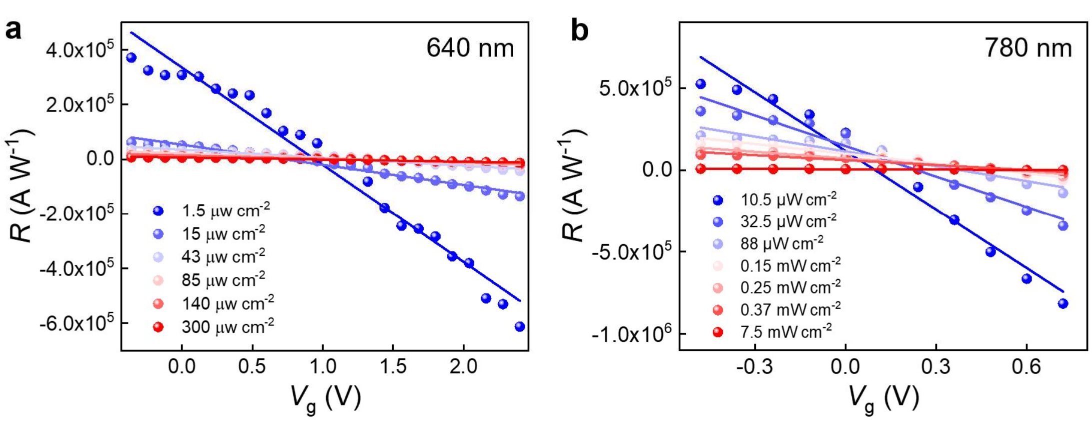

Supplementary Figure 7. Gate-voltage dependent bipolar photoresponsivity. Linear dependence of the bipolar photoresponsivity on the gate voltage under the light illumination of (a) 640 nm and (b) 780 nm.

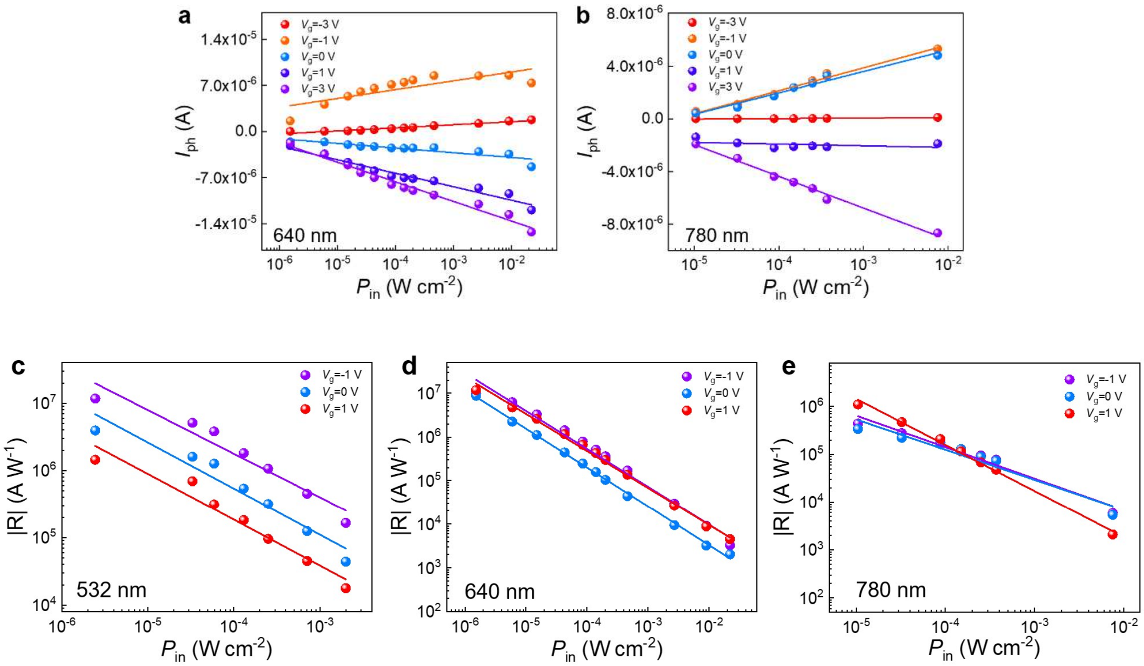

Supplementary Figure 8. Light intensity dependence of photocurrent and photoresponsivity at various gate voltages. Dependence of the net photocurrent on the light intensity under the light illumination of (a) 640 nm and (b) 780 nm with the gate voltage varying from -3 V to 3 V. Dependence of the photoresponsivity on the light intensity (c) 532 nm, (d) 640 nm, and (e) 780 nm, measured at the gate voltage of -1 V, 0 V and 1 V.

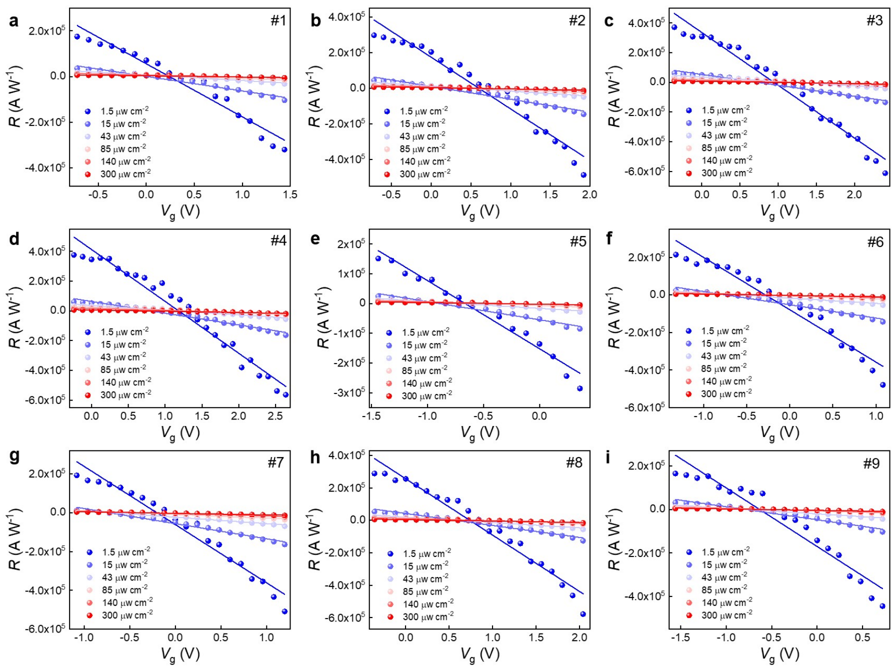

Supplementary Figure 9. Photoresponsivity uniformity of the phototransistor array. Linear photoresponsivity in response to the light intensity of the 3×3 $MAPbI_3/Bi_2O_2Se$ phototransistor array under 640 nm illumination across various gate voltages.

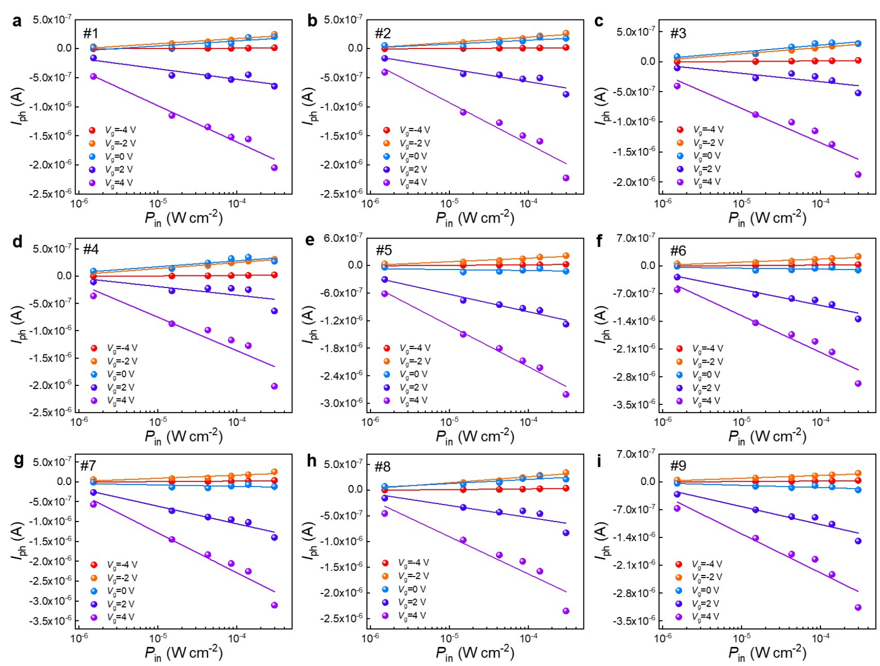

Supplementary Figure 10. Photocurrent uniformity of the phototransistor array. Photocurrent in response to the light intensity of the 3×3 $MAPbI_3/Bi_2O_2Se$ phototransistor array under 640 nm illumination across various gate voltages.

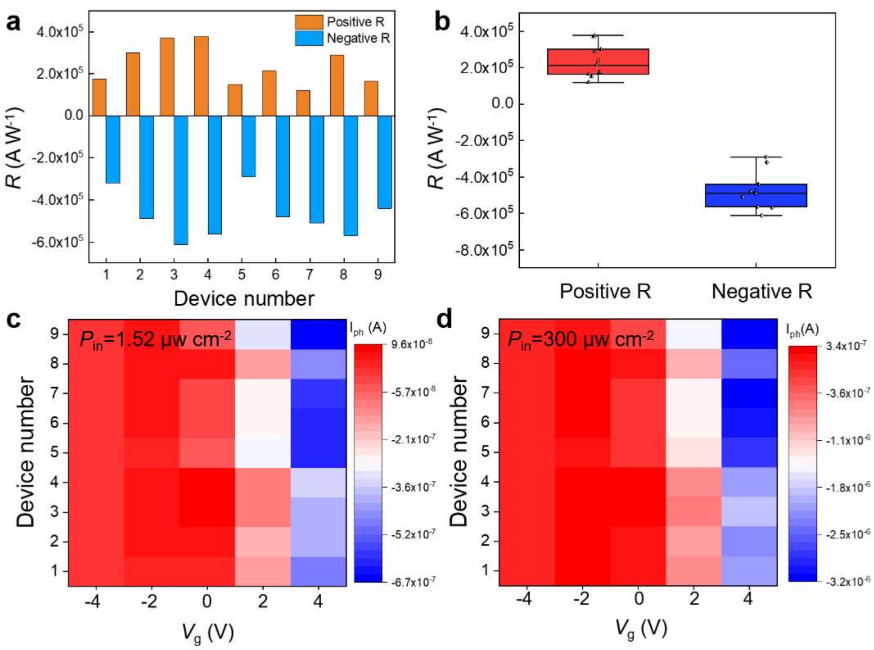

Supplementary Figure 11. Distributions of photoresponsivity and photocurrent. (a) Maximum positive and negative photoresponsivity of the 3×3 $MAPbI_3/Bi_2O_2Se$ phototransistor array. (b) Statistical distribution of maximum positive and negative photoresponsivity across the nine devices. The box represents the interquartile range, with the median indicated by the line inside the box. (c) Photocurrent distribution as a function of gate voltage across the nine devices at the light intensity of 1.52 μWcm^{-2}. (d) Photocurrent distribution as a function of gate voltage across the nine devices at the light intensity of 300 μWcm^{-2}.

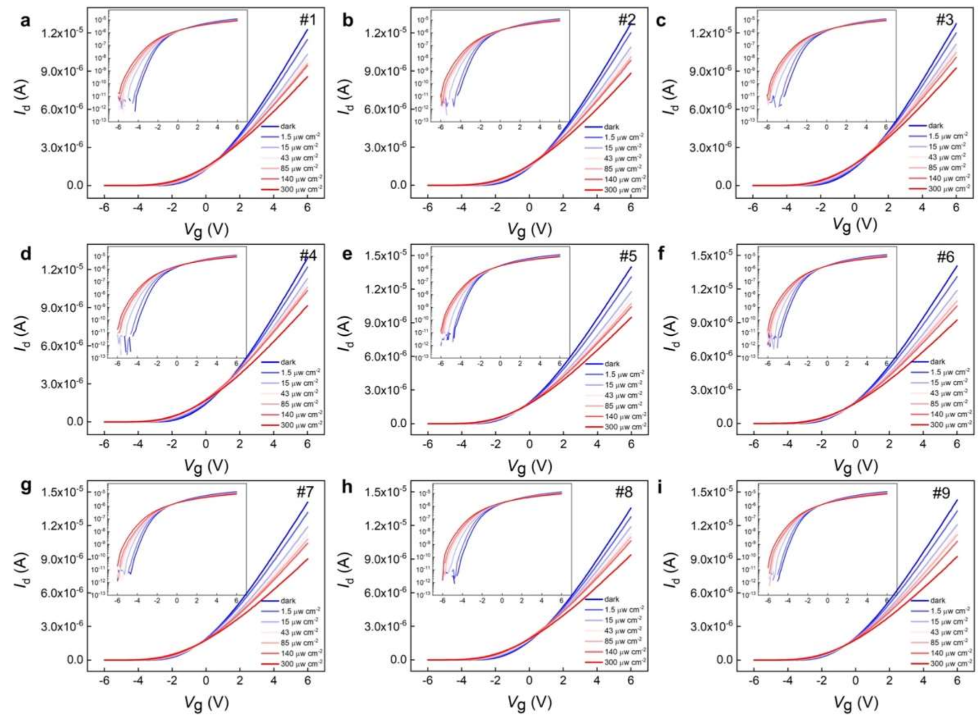

Supplementary Figure 12. Device uniformity in the heterotransistor array. Transfer curves of the $MAPbI_3/Bi_2O_2Se$ heterotransistor array under 640 nm illumination with varied light intensities tested after manufacturing. The inset images show the transfer curves on a logarithmic scale.

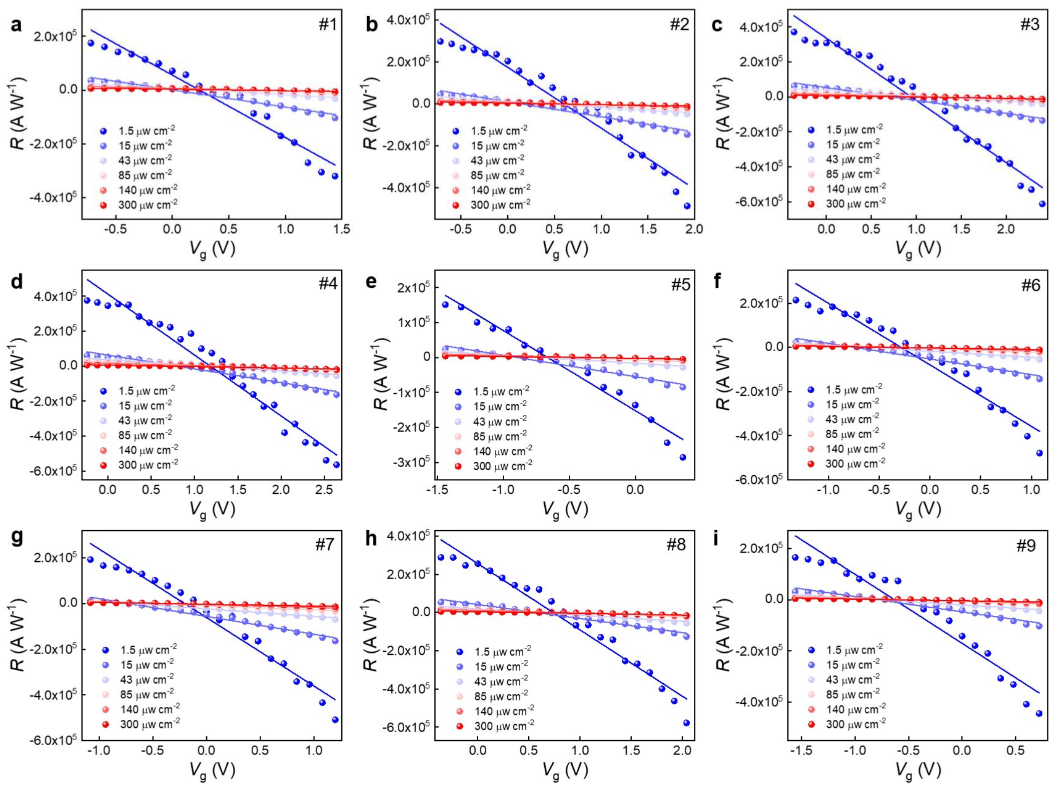

Supplementary Figure 13. Photoresponsivity uniformity of the phototransistor array. Linear dependence of the bipolar photoresponsivity on the gate voltage under 640 nm illumination with varied light intensities tested after manufacturing.

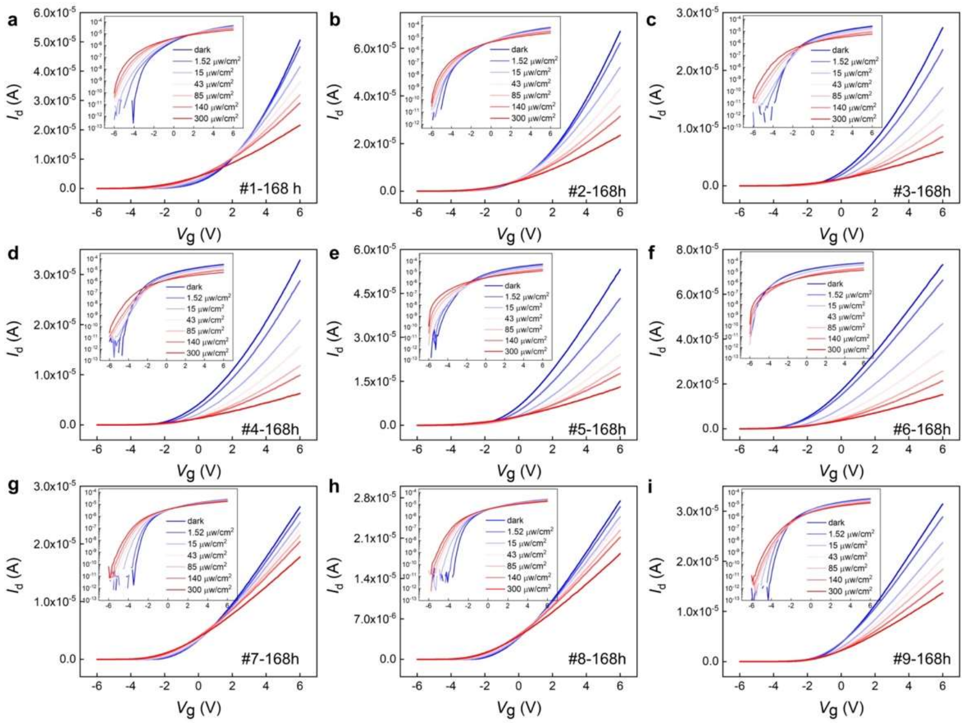

Supplementary Figure 14. Stability analysis of the phototransistor array. Transfer curves of the $MAPbI_3/Bi_2O_2Se$ heterotransistor array under 640 nm illumination with varied light intensities tested after one week at atmosphere. The inset images show the transfer curves on a logarithmic scale.

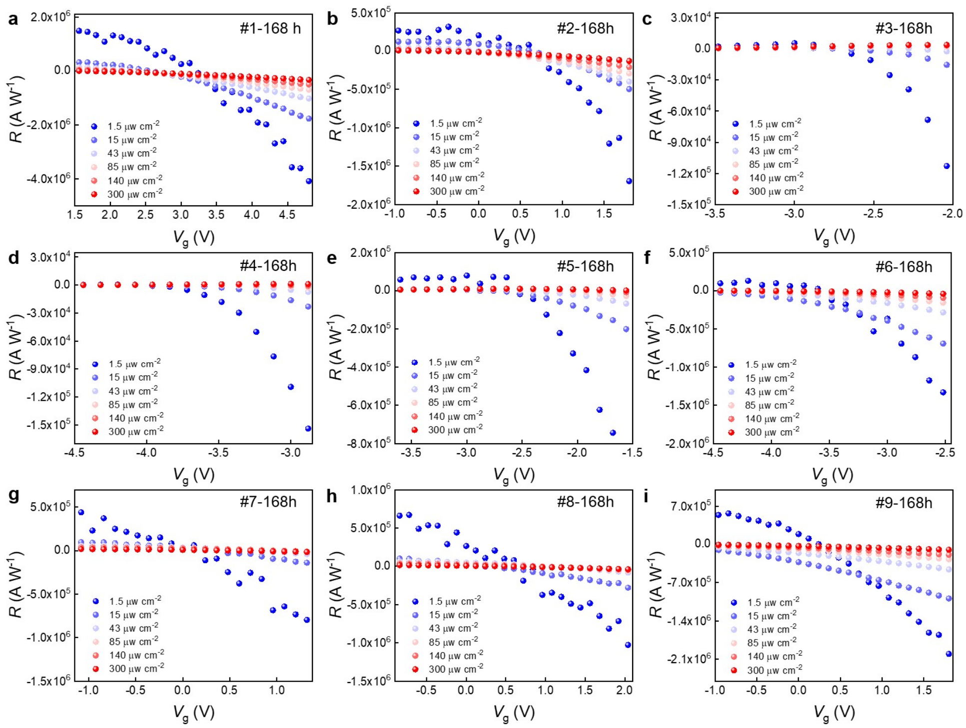

Supplementary Figure 15. Photoresponsivity Stability in the phototransistor array. Linear dependence of the bipolar photoresponsivity on the gate voltage under 640 nm illumination with varied light intensities tested after one week at atmosphere.

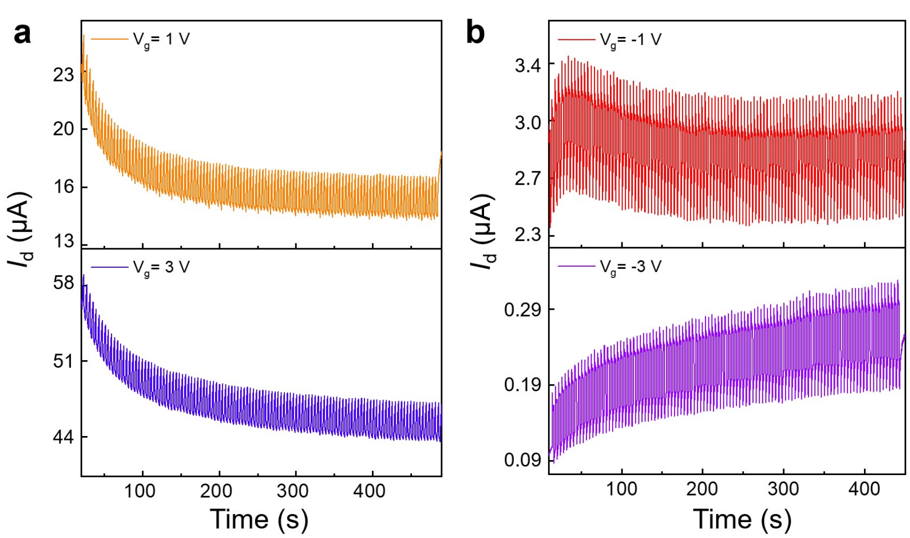

Supplementary Figure 16. Recycling tests of the bipolar heterotransistor. Recycling (a) negative and (b) positive photoresponses of $MAPbI_3/Bi_2O_2Se$ heterotransistor under the light illumination of 532 nm.

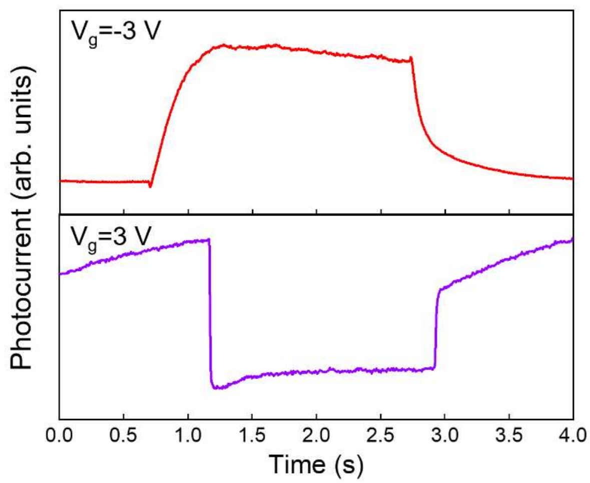

Supplementary Figure 17. Photoresponse time characteristics. Positive and negative photoresponse time of the $MAPbI_3/Bi_2O_2Se$ heterotransistor under the wavelength of 532 nm.

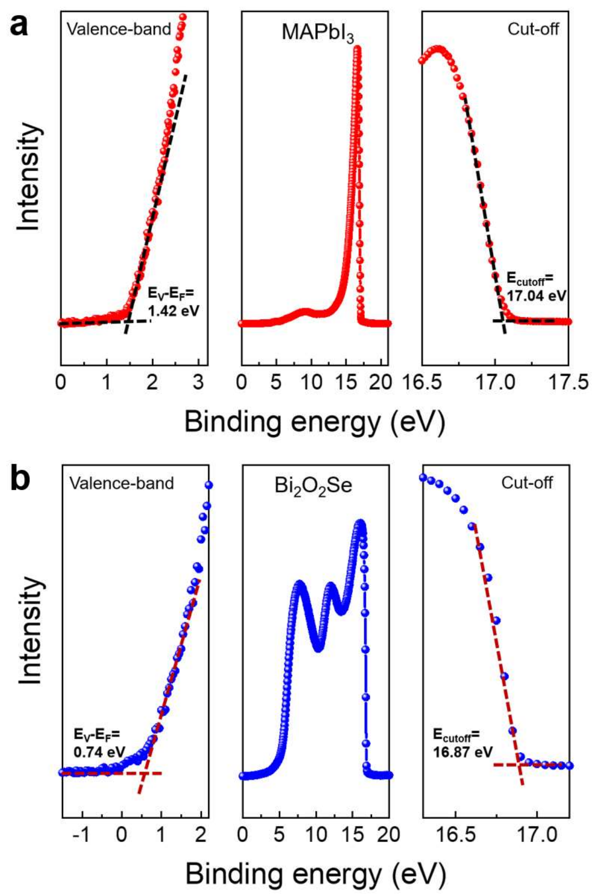

Supplementary Figure 18. Ultraviolet photoelectron spectroscopy characteristics. Ultraviolet photoelectron spectroscopy of (a) $MAPbI_3$ and (b) Bi_2O_2Se films.

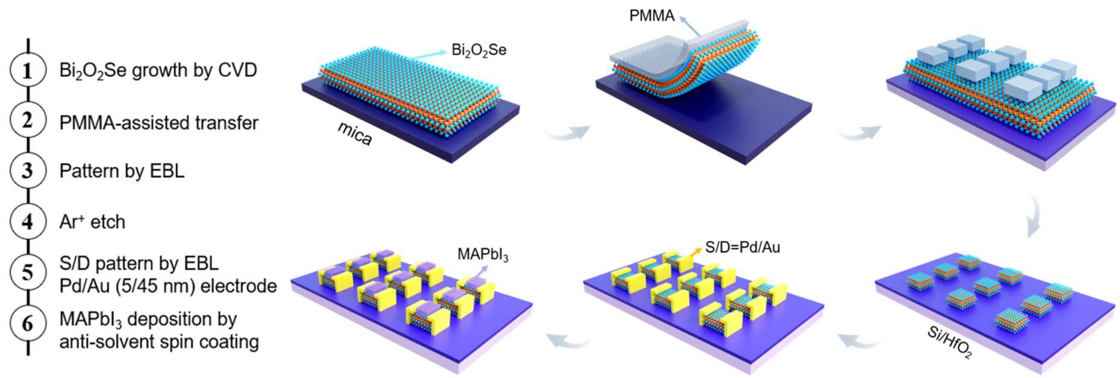

Supplementary Figure 19. Fabrication process of the heterotransistor array. Scheme of the manufacturing procedure of $MAPbI_3/Bi_2O_2Se$ heterotransistor array.

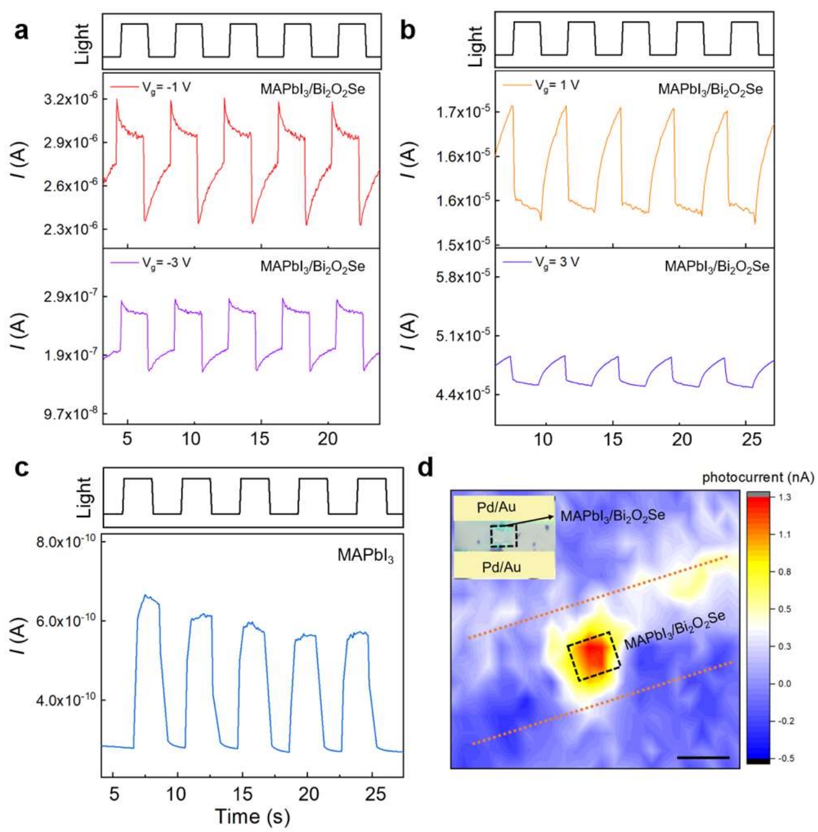

Supplementary Figure 20. Optoelectronic characteristics of the heterotransistor. (a) Positive photoresponses of the $MAPbI_3/Bi_2O_2Se$ heterotransistor under the gate voltage of V_g=-1 V and V_g=-3 V. (b) Negative photoresponses of the $MAPbI_3/Bi_2O_2Se$ heterotransistor under the gate voltage of V_g=1 V and V_g=3 V. (c) Photoresponses of single $MAPbI_3$ photosensor. (d) Photocurrent mapping of the $MAPbI_3/Bi_2O_2Se$ heterotransistor and its surrounding regions. All optoelectronic measurements were conducted using a 532 nm laser. The scale bar is 5 μm.

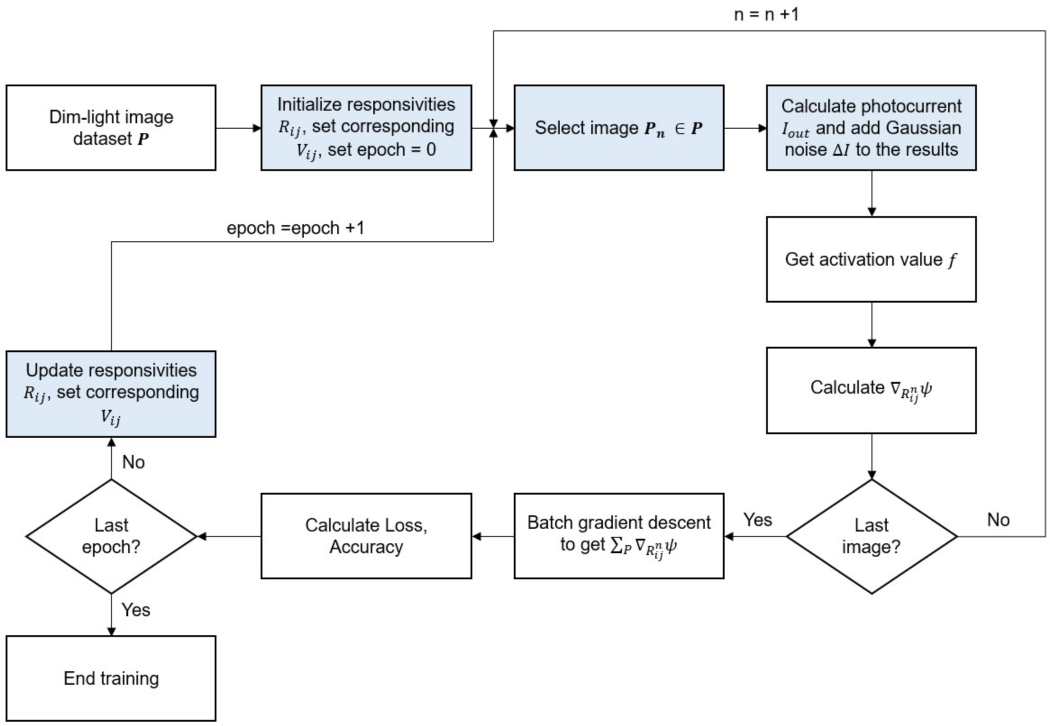

Supplementary Figure 21. Training algorithm for classifying. Flow chart illustrating the training algorithm for the letter classification task.

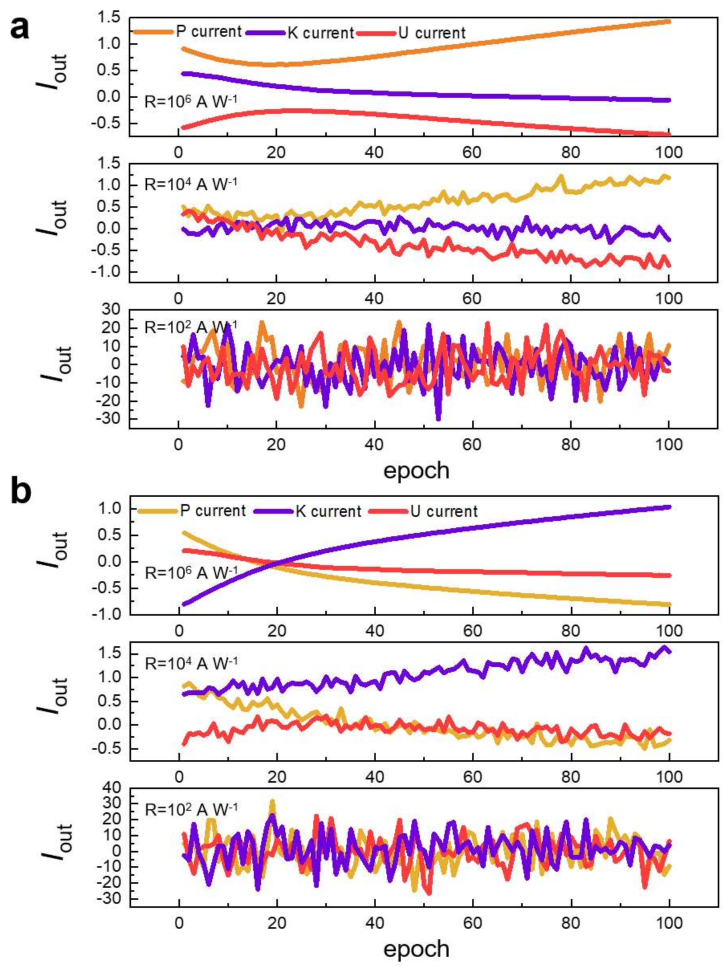

Supplementary Figure 22. Output photocurrents of the heterotransistor array for letter classification. Output photocurrents of the $MAPbI_3/Bi_2O_2Se$ heterotransistor array with varied photoresponsivities executing in-sensor analog multiply-accumulate operations for classifying the letter (a) "P" and (b) "K".

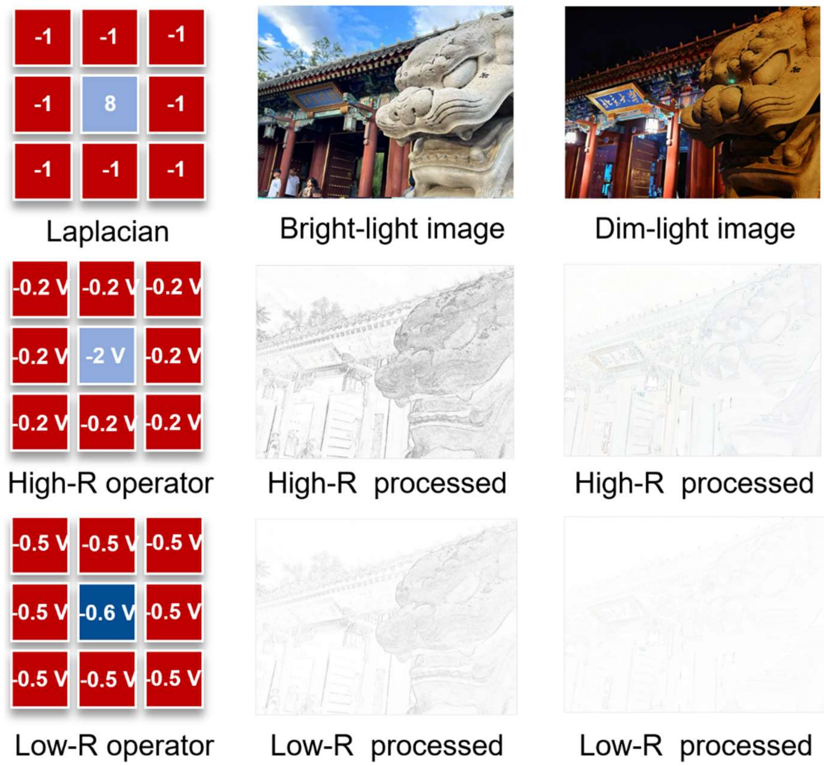

Supplementary Figure 23. Reconfigurable heterotransistor array for edge detection. Edge detection results for bright and dim images using the $MAPbI_3/Bi_2O_2Se$ reconfigurable sensor array with high photoresponsivities and low photoresponsivities, respectively.

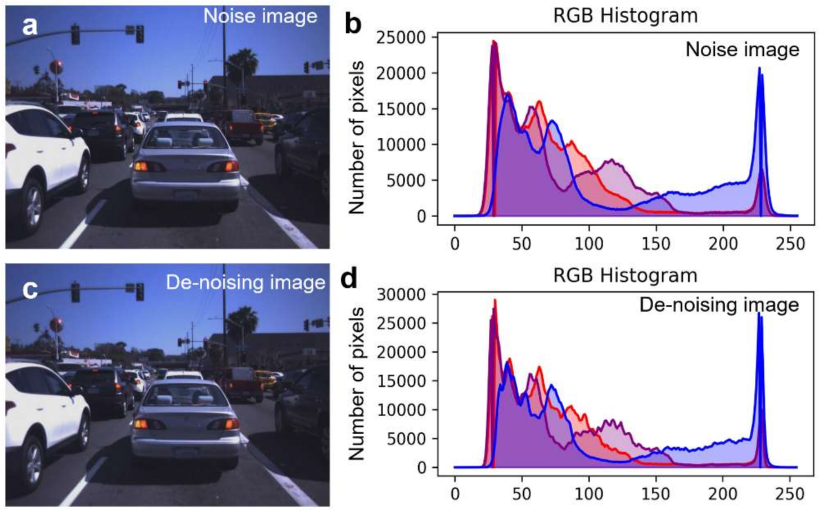

Supplementary Figure 24. Visual comparison of the images before and after noise reductions. (a) Original image with Gaussian noises. (b) Histogram of the noised image, showing a smooth and single-peaked distribution. (c) Image after denoising with improved detail and clarity. (d) Histogram of the denoised image, displaying a multi-peaked distribution that reflects the restoration of image details.

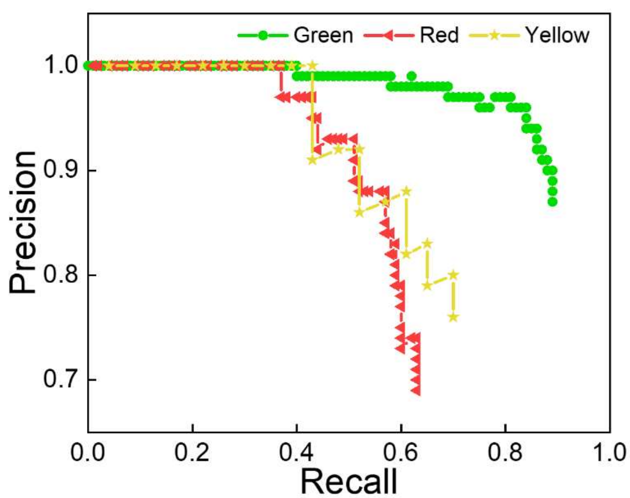

Supplementary Figure 25. Recall-precision curves. Precision comparation for green, red, and yellow traffic lights without preprocessing.

Supplementary References

1 Wu, J., Yuan, H., Meng, M., Chen, C., Sun, Y., Chen, Z., Dang, W., Tan, C., Liu, Y. & Yin, J. High electron mobility and quantum oscillations in non-encapsulated ultrathin semiconducting Bi_2O_2Se. *Nat. Nanotechnol.* **12**, 530-534 (2017).

2 Mosconi, E., Umari, P. & De Angelis, F. Electronic and optical properties of $MAPbX_3$ perovskites (X= I, Br, Cl): a unified DFT and GW theoretical analysis. *Phys. Chem. Chem. Phys*. **18**, 27158-27164 (2016).

3 Cheng, T., Tan, C., Zhang, S., Tu, T., Peng, H. & Liu, Z. Raman spectra and strain effects in bismuth oxychalcogenides. *J. Phys. Chem. C*. **122**, 19970-19980 (2018).

4 Huang, X., Niu, C.-Y., Zhang, J., Wang, A., Jia, Y. & Song, Y. Strain-tunable electronic structure, optical response, and high electron mobility of Bi_2O_2Se crystals. *APL Mater.* **7**, 8 (2019).

5 Afsari, M., Boochani, A. & Shirdel, F. Electronic and optical properties of two propounded compound in photovoltaic applications, $CsPbI_3$ and $CH_3NH_3PbI_3$: By DFT. *Optik*. **199**, 163360 (2019).

6 Saha, S., Jaiswal, V., Sharma, P. & Aswal, D. Evolution of SI base unit candela: Quantifying the light perception of human eye. *Mapan*. **35**, 563-573 (2020).

7 Elion, G. R. Electro-optics handbook. *CRC Press*. (2020).